

AN EXPONENTIAL DECLINE AT THE BRIGHT END OF THE $Z = 6$ GALAXY LUMINOSITY FUNCTION

CHRIS J. WILLOTT¹, ROSS J. MCLURE², PASCALE HIBON³, RICHARD BIELBY⁴, HENRY J. MCCrackEN⁵, JEAN-PAUL KNEIB⁶, OLIVIER ILBERT⁶, DAVID G. BONFIELD⁷, VICTORIA A. BRUCE², AND MATT J. JARVIS⁷,

Draft version October 30, 2018

ABSTRACT

We present the results of a search for the most luminous star-forming galaxies at redshifts $z \approx 6$ based on CFHT Legacy Survey data. We identify a sample of 40 Lyman break galaxies brighter than magnitude $z' = 25.3$ across an area of almost 4 square degrees. Sensitive spectroscopic observations of seven galaxies provide redshifts for four, of which only two have moderate to strong Ly α emission lines. All four have clear continuum breaks in their spectra. Approximately half of the Lyman break galaxies are spatially resolved in 0.7 arcsec seeing images, indicating larger sizes than lower luminosity galaxies discovered with the *Hubble Space Telescope*, possibly due to on-going mergers. The stacked optical and infrared photometry is consistent with a galaxy model with stellar mass $\sim 10^{10} M_{\odot}$. There is strong evidence for substantial dust reddening with a best-fit $A_V = 0.75$ and $A_V > 0.48$ at 2σ confidence, in contrast to the typical dust-free galaxies of lower luminosity at this epoch. The spatial extent and spectral energy distribution suggest that the most luminous $z \approx 6$ galaxies are undergoing merger-induced starbursts. The luminosity function of $z = 5.9$ star-forming galaxies is derived. This agrees well with previous work and shows strong evidence for an exponential decline at the bright end, indicating that the feedback processes which govern the shape of the bright end are occurring effectively at this epoch.

Subject headings: cosmology: observations — galaxies: evolution — galaxies: high-redshift

1. INTRODUCTION

The light from distant galaxies brings evidence of the conditions and physical processes at play in the early Universe. By studying the changes in galaxy properties over cosmic time we obtain a deeper understanding of how our Universe evolved. At 1 billion years after the Big Bang, galaxies were typically smaller, less luminous and less dusty than today (Bouwens et al. 2006). Such observations need to be explained by cosmological simulations which account for the hierarchical merging of dark matter halos and the gas accretion and cooling inside them necessary to form stars (e.g. Finlator et al. 2011).

One of the key measurements of the evolving Universe is the galaxy luminosity function. This function is related to the star formation rate occurring at an epoch and how the star formation is distributed across the galaxy population. Ultraviolet luminosity is well correlated with the formation rate of young, hot stars, with the caveat that dust extinction, common in starbursts, reduces the observed ultraviolet flux. Comparison of the observed lumi-

osity function with that predicted by models constrains the important physical processes occurring. For example, the faint end slope of the galaxy luminosity function at redshifts up to at least $z = 6$ is flatter than the dark matter halo mass function (Bouwens et al. 2007), which could be explained by feedback from supernovae winds (Cole 1991) or from photoevaporation and heating during reionization (Barkana & Loeb 2001). At the bright end, the galaxy luminosity declines much more sharply than the halo mass function. This is usually ascribed to AGN feedback and inefficient gas cooling in high mass halos (e.g. Benson et al. 2003).

Surveys for UV-continuum-selected galaxies at $z \gtrsim 6$ have been largely focused on *Hubble Space Telescope* due to the small sizes of the galaxies and low background in space. Hundreds of such galaxies have been identified in deep ACS imaging of the GOODS, Hubble Ultra Deep (HUDF) and parallel fields (Dickinson et al. 2004; Bunker et al. 2004; Yan & Windhorst 2004; Bouwens et al. 2006). The extremely deep imaging over the very small area of the HUDF identifies galaxies with absolute magnitude at 1350 Å, $M_{1350} = -18$, corresponding to a star formation rate of only $1 M_{\odot} \text{ yr}^{-1}$ (Kennicutt 1998). These *Hubble Space Telescope* surveys have led to a good description of the $z = 6$ luminosity function over the range $-21 < M_{1350} < -18$ (Bouwens et al. 2007, 2008; Su et al. 2011). The luminosity function can be fit by a Schechter function with characteristic break luminosity of $M_{1350} = -20.2$. However, the few sources detected brighter than the break leave the exact nature of the high-luminosity decline uncertain.

Several surveys have been carried out from the ground over wider areas to find the rarer, more luminous $z \approx 6$ galaxies. McLure et al. (2006, 2009) and Curtis-Lake et al. (2012) report on $5 < z < 6.5$ galaxies found within the 0.8 square degree Subaru/*XMM-Newton* Deep Sur-

¹ Herzberg Institute of Astrophysics, National Research Council, 5071 West Saanich Rd, Victoria, BC V9E 2E7, Canada; chris.willott@nrc.ca

² SUPA Institute for Astronomy, University of Edinburgh, Royal Observatory, Edinburgh EH9 3HJ, UK

³ Gemini Observatory, Gemini South, AURA/Chile, P.O. Box 26732, Tucson, AZ 85726, USA

⁴ Dept. of Physics, Durham University, South Road, Durham, DH1 3LE, UK

⁵ Institut d'Astrophysique de Paris, UMR7095 CNRS, Université Pierre et Marie Curie, 98 bis Boulevard Arago, 75014 Paris, France

⁶ Laboratoire d'Astrophysique de Marseille, Université Aix-Marseille, 38 rue Frédéric Joliot-Curie, 13388 Marseille, France

⁷ Centre for Astrophysics, Science and Technology Research Institute, University of Hertfordshire, Hatfield, Herts AL10 9AB, UK

vey (optical) and UKIDSS Ultra Deep Survey (near-IR). This SXDS/UDS work provides tighter constraints on the luminosity function at $-22 < M_{1350} < -21$ than from GOODS (McLure et al. 2009). Shimasaku et al. (2005), Nagao et al. (2007) and Jiang et al. (2011) have discovered many $z \approx 6$ galaxies in the 0.25 square degree Subaru Deep Field (SDF) which provides good luminosity function constraints for $-21 < M_{1350} < -20$. Together these works show that the galaxy luminosity function at $z = 6$ can be fit by a Schechter function, the same parameterization that successfully fits at lower redshift. The surveys discussed above only contain enough volume to discover galaxies with a space density of $\gtrsim 10^{-6} \text{ Mpc}^{-3}$. They show there is a steepening of the luminosity function, but do not confirm whether the cut-off is exponential or less steep than this.

At even higher redshifts ($z \sim 7 - 8$) there have been mixed results from ground-based surveys to determine the bright end of the luminosity function. Castellano et al. (2010) found a decrease in the space density from $z = 6$ to $z = 6.8$ of a factor of 3.5. Capak et al. (2011) found three UV-bright $z \sim 7$ galaxy candidates in the 2 square degree COSMOS field. Although there is some evidence that these galaxies are low- z interlopers, if they are truly at $z \approx 7$ then the galaxy luminosity function does not decline precipitously as a Schechter function, but rather as a power-law. Luminous $z \approx 8$ LBG candidates have recently been reported by Yan et al. (2011), also suggesting a bright end decline less steep than a Schechter function. Although both the above studies could be affected by low- z contamination, it is important to determine how well the $z = 6$ luminosity function is fit by a Schechter function, because there is little cosmic time available between $z = 6$ and $z = 7$ for significant evolution of the shape of the luminosity function. Capak et al. noted that their result could be explained if AGN feedback is less effective at early times due to the time required for supermassive black holes to build up their mass via Eddington-limited accretion and mergers.

The *Deep* component of the Canada-France-Hawaii Telescope Legacy Survey (CFHTLS⁸) provides the deepest optical data covering several square degrees and the largest area survey capable of finding $z \approx 6$ galaxies based on their rest-frame UV continuum. At a total of nearly 4 square degrees the volume probed is approximately 40 times that of the GOODS survey and five times the previous largest area studied, the SXDS/UDS. We present the results of a search for $z \approx 6$ galaxies in the CFHTLS. Section 2 describes the optical and near-IR data used and how the galaxies were selected. Section 3 gives details of spectroscopic followup of a subset of the galaxies. Section 4 considers the physical sizes of these galaxies. In Section 5 we stack together the optical and IR images for the galaxy sample to demonstrate their high- z nature and determine the typical galaxy SED. Section 6 presents the resulting luminosity function and our conclusions are drawn in Section 7.

All optical and near-IR magnitudes in this paper are on the AB system. Cosmological parameters of $H_0 = 70 \text{ km s}^{-1} \text{ Mpc}^{-1}$, $\Omega_M = 0.30$ and $\Omega_\Lambda = 0.7$ are assumed throughout. These parameters have been adopted to ease comparison with previous work, even though they are

slightly different from the best fit in Jarosik et al. (2011).

2. IMAGING AND SAMPLE SELECTION

2.1. Imaging observations

The imaging data used to select high-redshift galaxies come primarily from the 3.6 m Canada-France-Hawaii Telescope. Optical observations with MegaCam in the $u^*g'r'i'z'$ filters are from CFHTLS Deep which covered four ≈ 1 square degree fields with typical total integration time of 75 ks in u^* , 85 ks in g' , 145 ks in r' , 230 ks in i' and 175 ks in z' . The seeing in the final stacks at i' and z' range from 0.66 to 0.76 arcsec. The data used here are from the 6th data release, T0006, which contains all the data acquired over the five years of the project¹⁰.

These optical data are complemented by near-IR data from the WIRCam Deep Survey (WIRDS; Bielby et al. 2012). WIRDS used the WIRCam near-IR imager at the CFHT to cover 2.4 square degrees of the CFHTLS Deep reaching typical 50% completeness depth of AB magnitude 24.5 in the JHK_s filters. A few high-redshift galaxy candidates not in the regions covered by WIRDS had J band photometry obtained from the Gemini-North Telescope using GNIRS and from the ESO New Technology Telescope using SOFI. More recently, near-IR data for some of these regions has become available from the ESO VISTA telescope. The D1 and D2 fields are fully covered by the first public data releases of the VIDEO survey (Jarvis et al. 2012) and UltraVISTA survey (McCracken et al. 2012), respectively. These data reach about a magnitude deeper than WIRDS, so all sources in D1 and D2 have $YJHK$ photometry in this paper from the VISTA surveys instead of the original WIRDS data. Note that the VIDEO data used has been corrected for the non-optimal sky subtraction detailed in the release notes. Small parts of the D2 and D3 field are covered by the *Hubble Space Telescope* Multi-Cycle Treasury program CANDELS (Grogin et al. 2011; Koekemoer et al. 2011).

Photometry was carried out in dual-image mode using the SExtractor source extractor software (Bertin & Arnouts 1996). The z' band was used as the detection band because it provides the highest signal-to-noise (S/N) for $z \approx 6$ galaxies. 2 arcsec diameter photometric apertures were used. Aperture magnitudes were corrected to total magnitudes assuming that the objects are spatially unresolved. This gives a lower limit on the flux for spatially extended objects.

2.2. Sample Selection

There are two methods for selecting high-redshift galaxies from optical/IR broad-band imaging, Lyman break and photometric redshifts. The Lyman break technique adopts hard color cuts in one or more colors possibly including non-detections in certain filters, whereas photometric redshifts use all available filters to derive a redshift probability distribution. Photometric redshifts are most suitable when the targets will be detected in many filters. However they reduce to a Lyman break-type selection if only a few filters are deep enough to constrain the relevant objects. In this work we use the Lyman break technique for homogeneous selection be-

⁹ <http://www.cfht.hawaii.edu/Science/CFHTLS>

¹¹ http://terapix.iap.fr/rubrique.php?id_rubrique=259

cause of the variable near-IR data quality in the different Deep fields.

We set a magnitude limit of $z' < 25.3$ to ensure that the objects are real and not too faint for good photometry. Over most of the survey area this limit corresponds to a 7σ detection in our 2 arcsec apertures. It will be shown in Section 2.3 that for the fields with the deepest near-IR data (D1 and D2) all 39 z' selected objects (galaxies and brown dwarfs) have a counterpart at i' and/or J , showing the rate of spurious z' band detections in the sample is very low. The high z' threshold ($\approx 7\sigma$) minimizes the problem of photometric scatter of objects into our sample with true colors different from the selection criteria. The luminosity function has been well studied by others at magnitudes fainter than this limit. The primary selection criterion is color $i' - z' > 2$ which corresponds to the break across the Ly α line. This criterion is somewhat stricter than other studies (e.g. Bouwens et al. 2006; Jiang et al. 2011) but ensures that contamination from low redshift galaxies and brown dwarfs is kept to a minimum. Two of our objects lie in slightly less deep than average regions at i' band and are undetected at i' with measured limits of $i' - z' > 1.97$ and $i' - z' > 1.99$. These are included in the sample because there is a high likelihood they would have $i' - z' > 2$ if deeper i' data were available.

Most Lyman break surveys adopt two colour criteria and therefore define a box in two-dimensional color-color space. We adopt a similar, but slightly different, method. Instead of a hard cut-off in $z' - J$ color we consider all the properties of every source in the $i' - z' > 2$ selection region and determine whether it is most likely a high-redshift galaxy or something else. This is important here because the CFHTLS Deep Fields contain varying amounts of extra multi-wavelength data which can be used as an additional constraint.

The initial automated search routine revealed 136 possible candidates brighter than the magnitude limit and having $i' - z' > 2$ in the ~ 4 square degrees CFHTLS Deep. The images were inspected by eye. Sometimes more detailed manual photometry for objects in locations with varying background was performed. Non-detections in the CFHTLS $u^*g'r'$ filters were also required for good LBG candidates. We checked that this criterion would not eliminate true LBGs using the model galaxy simulations to be described in Section 6.1 that account for the observed variation of galaxy and intergalactic medium (IGM) properties. It was found that only 0.02% of galaxies at $5.7 < z < 6.0$ have colors $r' - z' < 3.5$ and hence could potentially be detected at r' band (typical 2σ limit is $r' \sim 27.5$ to 28) for the brightest galaxies that have $z' \approx 24.5$. The most common problems leading to rejection from the sample were due to structured background near bright stars or close to the edges of the fields where the effective exposure time is lower. A total of 69 candidates were removed from the list in this process. This left 67 true astronomical sources with $i' - z' > 2$.

For each of these, the available data was studied to determine its nature. The primary filter for this process is J because brown dwarfs are known to have much higher $z' - J$ colors than high-redshift galaxies. 7 of the 67 sources do not have J band coverage. The next most important is K_s band because reddened galaxies at $z \approx 1$ would be expected to be bright at K_s . In addi-

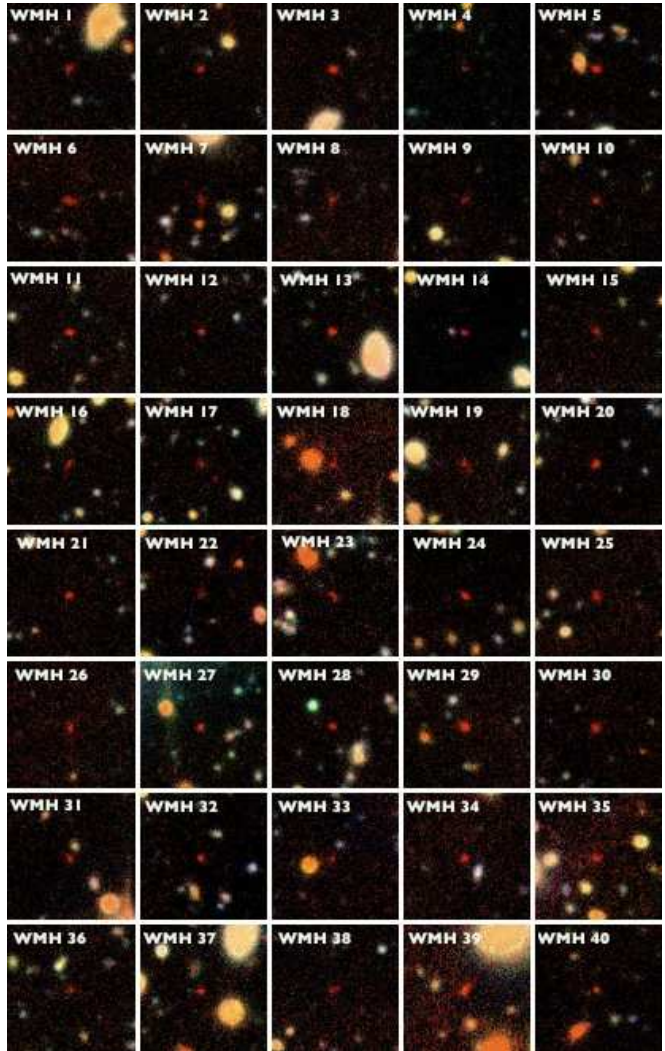


Figure 1. Color images ($r'i'z'$) for the sample of 40 $z \approx 6$ Lyman break galaxies. Each image covers $15'' \times 15''$ and is oriented with north up and east to the left. The LBGs are the small red objects at the centers. Some are clearly spatially extended.

tion, three of the fields have at least partial *Spitzer Space Telescope* IRAC coverage available from SWIRE (Lonsdale et al. 2003), S-COSMOS (Sanders et al. 2007) and AEGIS (Barmby et al. 2008). The COSMOS field also has deep Subaru imaging with broad-band depth similar to CFHTLS, additional medium-band filters (Taniguchi et al. 2007) and HST F814W imaging (Scoville et al. 2007) which is useful for compact sources.

As discussed in the following section, the results of this process showed that 40 of the 67 candidates were most likely $z \approx 6$ Lyman break galaxies and the remaining 27 are most likely to be brown dwarfs.

2.3. Evidence for $z \approx 6$ galaxies

Three-colour ($r'i'z'$) images for the the 40 candidates classified as high-redshift galaxies are shown in Figure 1. Photometric measurements in the $i'z'J$ filters are given in Table 1. In the case that an object is not detected, a magnitude limit is given. These magnitude limits are determined from the variance of photometric aperture fluxes at random locations close to the object. At i'

Table 1
Position and photometry of CFHTLS $z = 6$ Lyman break galaxies

| Name | R.A. and Decl. (J2000.0) | i' mag | z' mag | J mag | $i' - z'$ | $z' - J$ | FWHM (arcsec) |
|--------|--------------------------|--------------|--------------|--------------|-----------|----------|---------------|
| WMH 1 | 02:24:13.79 -04:56:41.4 | 27.18 ± 0.26 | 25.15 ± 0.10 | > 25.00 | 2.02 | < 0.15 | 1.36 |
| WMH 2 | 02:24:15.10 -04:20:47.0 | 27.29 ± 0.29 | 25.14 ± 0.10 | 24.58 ± 0.24 | 2.14 | 0.56 | 0.92 |
| WMH 3 | 02:24:51.14 -04:03:29.4 | 27.42 ± 0.32 | 24.78 ± 0.07 | 24.57 ± 0.24 | 2.63 | 0.21 | 0.94 |
| WMH 4 | 02:25:19.64 -04:28:06.8 | 27.47 ± 0.42 | 25.21 ± 0.13 | > 25.30 | 2.26 | < -0.09 | 0.88 |
| WMH 5 | 02:26:27.03 -04:52:38.3 | 27.47 ± 0.34 | 24.54 ± 0.06 | 24.17 ± 0.17 | 2.92 | 0.37 | 1.11 |
| WMH 6 | 02:27:18.77 -04:50:08.4 | 26.97 ± 0.22 | 24.85 ± 0.08 | 25.16 ± 0.39 | 2.11 | -0.31 | 1.94 |
| WMH 7 | 02:27:29.03 -04:33:04.3 | 27.69 ± 0.48 | 25.26 ± 0.11 | 24.87 ± 0.31 | 2.42 | 0.39 | 1.45 |
| WMH 8 | 02:27:46.20 -04:30:32.2 | 27.46 ± 0.34 | 25.16 ± 0.10 | 24.35 ± 0.20 | 2.29 | 0.81 | 1.73 |
| WMH 9 | 09:58:45.49 +02:23:24.8 | 27.67 ± 0.49 | 25.27 ± 0.12 | 24.84 ± 0.30 | 2.39 | 0.43 | 1.21 |
| WMH 10 | 09:58:59.84 +01:59:48.8 | 27.42 ± 0.37 | 25.24 ± 0.12 | 25.16 ± 0.39 | 2.18 | 0.08 | 0.84 |
| WMH 11 | 09:59:44.49 +02:09:36.7 | 27.29 ± 0.33 | 25.06 ± 0.10 | 24.90 ± 0.32 | 2.23 | 0.16 | 1.02 |
| WMH 12 | 09:59:52.74 +02:25:53.2 | 27.34 ± 0.41 | 25.17 ± 0.13 | 25.03 ± 0.35 | 2.17 | 0.13 | 0.99 |
| WMH 13 | 09:59:56.54 +02:12:27.1 | 26.78 ± 0.21 | 24.78 ± 0.08 | 24.53 ± 0.23 | 2.00 | 0.25 | 0.86 |
| WMH 14 | 10:00:19.93 +02:25:36.8 | 26.98 ± 0.26 | 24.88 ± 0.09 | 24.83 ± 0.07 | 2.09 | 0.05 | 0.74 |
| WMH 15 | 10:00:26.37 +02:13:46.8 | > 27.35 | 24.99 ± 0.10 | 24.68 ± 0.07 | > 2.35 | 0.31 | 1.24 |
| WMH 16 | 10:00:30.58 +02:19:35.1 | 27.56 ± 0.42 | 25.27 ± 0.12 | 24.51 ± 0.07 | 2.28 | 0.76 | 1.11 |
| WMH 17 | 10:00:50.10 +02:13:03.3 | 27.37 ± 0.38 | 25.17 ± 0.12 | 24.60 ± 0.25 | 2.20 | 0.57 | 1.05 |
| WMH 18 | 10:00:59.82 +01:57:26.6 | > 27.27 | 25.24 ± 0.15 | 24.63 ± 0.26 | > 2.02 | 0.61 | 1.10 |
| WMH 19 | 10:01:18.99 +02:11:11.6 | 27.64 ± 0.46 | 25.15 ± 0.11 | > 25.20 | 2.48 | < -0.05 | 1.29 |
| WMH 20 | 10:01:21.54 +02:12:22.5 | 26.83 ± 0.22 | 24.65 ± 0.07 | 24.14 ± 0.17 | 2.18 | 0.51 | 0.86 |
| WMH 21 | 10:01:21.94 +02:19:37.6 | 27.20 ± 0.30 | 25.12 ± 0.10 | 24.15 ± 0.17 | 2.07 | 0.97 | 1.25 |
| WMH 22 | 10:01:38.37 +01:43:48.1 | 27.43 ± 0.45 | 25.28 ± 0.13 | > 25.20 | 2.14 | < 0.08 | 0.81 |
| WMH 23 | 10:01:38.71 +02:28:20.0 | > 27.16 | 25.05 ± 0.12 | 24.31 ± 0.19 | > 2.10 | 0.74 | 1.32 |
| WMH 24 | 14:16:20.38 +52:13:23.4 | > 27.07 | 24.72 ± 0.07 | — | > 2.34 | — | 1.03 |
| WMH 25 | 14:17:47.97 +52:38:09.4 | > 27.28 | 25.04 ± 0.10 | > 25.19 | > 2.23 | < -0.15 | 1.53 |
| WMH 26 | 14:18:10.47 +52:19:43.4 | 27.79 ± 0.45 | 25.13 ± 0.10 | — | 2.65 | — | 1.24 |
| WMH 27 | 14:18:40.04 +52:35:08.2 | 27.20 ± 0.32 | 25.09 ± 0.10 | > 24.61 | 2.10 | < 0.48 | 1.15 |
| WMH 28 | 14:18:52.23 +53:07:47.3 | 27.31 ± 0.29 | 25.23 ± 0.11 | > 24.16 | 2.08 | < 1.07 | 1.00 |
| WMH 29 | 14:19:20.53 +52:52:38.7 | 26.52 ± 0.14 | 24.41 ± 0.05 | 24.42 ± 0.05 | 2.10 | -0.01 | 1.11 |
| WMH 30 | 14:20:40.80 +52:52:45.3 | 27.47 ± 0.34 | 24.72 ± 0.07 | > 24.75 | 2.75 | < -0.03 | 1.08 |
| WMH 31 | 14:21:03.74 +52:12:16.2 | 26.90 ± 0.21 | 24.87 ± 0.08 | — | 2.02 | — | 1.08 |
| WMH 32 | 22:13:42.68 -17:56:33.2 | 27.42 ± 0.38 | 25.01 ± 0.10 | > 24.44 | 2.41 | < 0.57 | 0.77 |
| WMH 33 | 22:14:06.97 -17:37:59.7 | > 27.21 | 25.24 ± 0.13 | — | > 1.96 | — | 0.73 |
| WMH 34 | 22:14:46.63 -17:39:22.2 | 27.31 ± 0.35 | 24.98 ± 0.11 | — | 2.33 | — | 1.02 |
| WMH 35 | 22:15:04.28 -17:57:20.5 | > 27.18 | 25.03 ± 0.12 | > 24.48 | > 2.14 | < 0.55 | 1.44 |
| WMH 36 | 22:15:48.91 -17:35:45.7 | 27.30 ± 0.34 | 25.27 ± 0.14 | > 24.85 | 2.02 | < 0.42 | 1.17 |
| WMH 37 | 22:16:26.67 -18:04:45.0 | > 27.25 | 25.26 ± 0.13 | > 24.12 | > 1.98 | < 1.14 | 0.69 |
| WMH 38 | 22:16:38.04 -17:37:00.9 | 27.50 ± 0.44 | 25.21 ± 0.14 | > 24.85 | 2.29 | < 0.36 | 0.73 |
| WMH 39 | 22:17:08.83 -17:38:43.9 | 26.86 ± 0.24 | 24.61 ± 0.08 | 24.57 ± 0.26 | 2.25 | 0.04 | 1.53 |
| WMH 40 | 22:17:13.55 -18:11:45.7 | 27.15 ± 0.34 | 25.03 ± 0.10 | — | 2.11 | — | 0.80 |

Notes. All magnitudes are on the AB system. i' and z' photometry is from CFHTLS. J photometry is from VIDEO for D1, UltraVISTA for D2 and WIRDS for D3 and D4. Exceptions are WMH 14, WMH 15, WMH 16 and WMH 29 which uses CANDELS J data. Spatial size (FWHM) is measured on the CFHTLS z' images.

band, many sources appear to be marginally detected. Therefore i' magnitudes are quoted down to magnitude errors of 0.5 magnitudes, rather than the strict 2σ limits which are often brighter. This should be kept in mind if using i' magnitudes or $i' - z'$ colors from Table 1. Note that six of the 40 galaxies do not have J band observations. The evidence in favor of these being high-redshift galaxies will be discussed later. The final column gives the measured FWHM in the z' band. Many of the galaxies appear more extended than the seeing, a fact that will be discussed later.

Figure 2 shows the distribution of points on the $i' - z'$ vs $z' - J$ color-color diagram for the 60 of 67 candidates which are covered by J band observations. Almost all the sources detected at J band have colors close to the expected loci of $z > 5.7$ Lyman break galaxies or brown dwarfs. The derivation of the brown dwarf locus is given in Delorme et al. (2008). Close to the $i' - z' = 2$ boundary the dwarfs tend to lie below the line. A similar tendency was noted for the Canada-France Brown Dwarf Survey (Reyl   et al. 2010) and is at least partially due to photometric scatter of somewhat bluer dwarfs with intrinsic $i' - z' \approx 1.5$. Note that a similar effect will occur

for the high-redshift galaxies. This is why we began with a relatively high $i' - z'$ cut, so that even those scattered from lower $i' - z'$ have intrinsic colors matching only brown dwarfs or high- z galaxies. The brown dwarfs in the CFHTLS/WIRDS survey also have well-defined loci in the $z' - J$ vs $J - H$ and $J - H$ vs $H - K_s$ diagrams with no significant outliers.

The gray circles show colors of model galaxies at $0.5 < z < 3$ determined using the 2008 stellar population synthesis models of Charlot & Bruzual (priv. comm.). Passively evolving and dusty star-forming galaxies with ages ranging from a million years to the age of the universe at that redshift are included. Extreme dust extinction with optical depth up to $\tau = 10$ is included, because extreme dust is required to get such large $i' - z'$ colors. Note that due to the larger wavelength difference between z' and J than between i' and z' , the effect of extreme dust reddening is to push low- z galaxies into the brown dwarf region of the diagram. A combination of extreme reddening plus high photometric scatter would be required to obtain the colors of our sample. The low- z galaxy models closest to the location of the LBGs have $z \approx 1.2$ and $\tau \approx 10$. Such galaxies would be extremely rare and

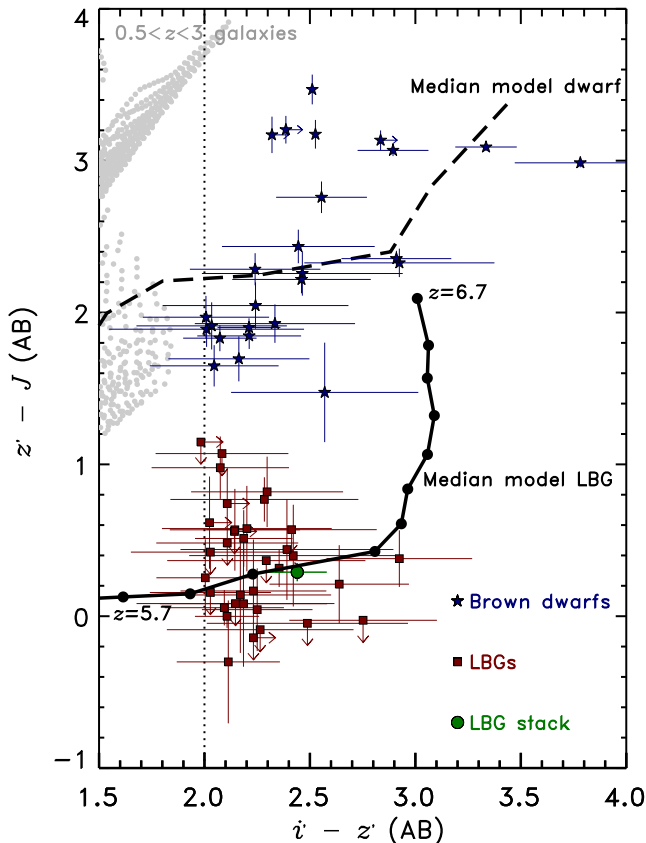


Figure 2. Color-color diagram for the $i' - z' > 2$ sources with $i' z' J$ imaging. Those classified as $z \approx 6$ LBGs are plotted as red squares whereas those classified as brown dwarfs are plotted as blue star symbols. The colors of the stacked LBG (Section 5) are shown with a large green circle. The thick black dashed line labeled “Median model dwarf” is the expected locus for brown dwarfs based on measurements of closer brown dwarfs. The “Median model LBG” curve shows the typical colors expected for LBGs with a range of UV continuum slope and Ly α emission, as described in Section 6.1. The gray circles show the possible colors for simulated galaxies at redshifts $0.5 < z < 3$ (see text for details).

faint.

21 of the 34 LBG-classified targets with J band data are detected at J . The other 13 have $z' - J$ limits well separated from the regions covered by brown dwarfs and reddened $0.5 < z < 3$ galaxies. We expect almost all the red squares in Figure 2 to be high-redshift galaxies as discussed below.

As noted in Table 1, many of the LBGs appear spatially resolved at z' band. Section 4 discusses this in much more detail and it is concluded that at least half of the LBGs are spatially resolved from the ground. In addition, *Hubble Space Telescope* observations of a subset also show that they are resolved. This provides further evidence against contamination by brown dwarfs.

A final source of contamination to consider is that by quasars at $z \approx 6$ which will have similar colors. A search for such quasars going to magnitude $z' < 24.5$ found none in the CFHTLS Deep survey area (Willott et al. 2010), but one at $z = 6.01$ with magnitude $z' = 24.4$ in the SXDS/UDS (McLure et al. 2006; Willott et al. 2009). At such faint magnitudes, the quasar luminosity function

slope is likely to be fairly flat (Willott et al. 2010), so the expectation would be for ≈ 1 more quasar in the magnitude range $24.5 < z' < 25.3$ across the full survey region.

2.4. Sources without J photometry

7 of the 67 $i' - z' > 2$ sample do not have J photometry because they lie outside the WIRDS and VISTA surveys and their nature, high- z galaxy or brown dwarf, had to be ascertained using other available information. Given the ratio of galaxies to brown dwarfs in the regions with J photometry we would expect 4 of these to be galaxies and 3 to be brown dwarfs.

One object is in the D4 field and a WIRCam K_s band image provided by Genevieve Soucail shows it to have $K_s = 22$. This red color of $z' - K_s = 2.8$ is consistent with a L dwarf.

The six remaining objects are retained in the list of likely $z \approx 6$ galaxies. WMH 24, WMH 26, WMH 31 and WMH 34 have measured z' band FWHM > 1 arcsec and therefore appear to be spatially resolved. As will be discussed in Section 4, only 15% of brown dwarfs are found to have such high FWHM. The probability that none of these four are brown dwarfs based on the FWHM argument is therefore 60%. WMH 33 has FWHM=0.73, so is consistent with being unresolved. However it is faint at z' band with $z' = 25.25$ and most sources close to the detection limit are galaxies. It is not detected in a WIRCam K_s band image that reaches to $K_s = 22$. If it were a L dwarf it would be expected to have $K_s \approx 22$ to 22.5, so this limit, although not definitive, suggests that it may be a galaxy. Therefore it is retained in the galaxy sample. WMH 40 has FWHM=0.80 arcsec and $z' = 25.05$. It is retained within the galaxy sample but we note it has almost equal probability to be a high- z galaxy, or a brown dwarf with these properties. In conclusion, at least four of these six objects are likely high- z galaxies. Taking into consideration there could be one $z \approx 6$ quasar in our sample, the contamination of our $z \approx 6$ galaxy sample is most likely $< 10\%$.

3. SPECTROSCOPY

3.1. Observations

The photometrically-selected high- z galaxies are spread across nearly 4 square degrees. Given that the typical field-of-view of multi-object spectrographs on large telescopes is $\ll 1$ degree, there is little opportunity for a high-multiplex factor. Spectroscopic observations have been attempted for 7 of the 40 candidates. Priority was given to those which are brightest at z' band to minimise the integration time required. All spectroscopy was performed using the GMOS spectrographs on the 8.2m Gemini Telescopes. The R400 gratings were used with 1 arcsec slits to give a resolution of $R = 1000$. CCD pixels were binned by a factor of two in the spectral direction so that each binned pixel covers 1.34 Å. WMH 13 was observed in long-slit mode, WMH 29 was observed equally in long-slit and multi-object mode, and all other observations used multi-object mode. Occasionally, two $z \approx 6$ galaxies could be fit on the same mask. The masks were filled with lower redshift Lyman break galaxies and photometric redshift selected galaxies ($z > 3.5$). All observations used the nod-and-shuffle mode to ensure good

Table 2
GMOS spectroscopy of $z \approx 6$ Lyman break galaxies

| Name | Integ. (hr) | M_{1350} | z_{spec} | QF ^a | $W_{\text{Ly}\alpha}$ ^b (Å) | $\text{HWHM}_{\text{Ly}\alpha}$ ^c (km s^{-1}) |
|----------|-------------|------------|-------------------|-----------------|----------------------------------------|---------------------------------------------------------------------|
| WMH 5 | 2.5 | -22.65 | 6.068 | A | 13 ± 4 | 220 ± 30 |
| WMH 6 | 2.5 | -21.75 | 5.645 | C | — | — |
| WMH 13 | 2.5 | -22.06 | 5.983 | A | 27 ± 8 | 210 ± 50 |
| WMH 15 | 4.0 | -21.98 | 5.847 | C | — | — |
| WMH 29 | 5.0 | -22.27 | 5.757 | B | 4 ± 2 | unres.? |
| WMH 34 | 2.3 | -21.67 | 5.759 | C | — | — |
| WMH 39 | 2.0 | -22.06 | 5.733 | B | — | — |
| Serendip | 2.5 | -21.33 | 5.618 | A | 31 ± 11 | 240 ± 40 |

^a QF is the Quality Flag of the redshift determination. See text. Note that QF=C redshifts are uncertain and z_{spec} merely gives the best fit redshift.

^b $\text{Ly}\alpha$ rest-frame equivalent width, quoted only if $\text{Ly}\alpha$ is detected. Uncertainties in $W_{\text{Ly}\alpha}$ are dominated by continuum placement.

^c Half-width half-maximum of the $\text{Ly}\alpha$ line measured from the peak to the red side of the line. These values have been deconvolved for the instrumental dispersion. The measured $\text{HWHM}_{\text{Ly}\alpha}$ for WMH 29 is 150 ± 60 , which is equal to the instrumental dispersion, but with significant uncertainty due to its low equivalent width.

subtraction of the sky background spectrum.

The long-slit observations were performed in queue-mode in excellent conditions in 2009. The multi-object observations were performed in classical mode on the nights of 12 December 2010, 27 and 28 June 2011 in variable conditions. Details of the spectroscopic observations and results are given in Table 2. Due to the faintness of these targets, the typical continuum S/N per pixel between 8500 Å and 9000 Å was only ~ 0.5 . Therefore, redshifts could only be quickly and unambiguously determined for the few sources which showed very strong $\text{Ly}\alpha$ emission lines. However, even at S/N = 0.5 per pixel, the continuum can be significantly detected over broader wavelength intervals and redshifts determined from continuum breaks (Spinrad et al. 1998).

3.2. Model fitting

To fully utilize the spectral information, a routine was developed to fit the observed spectrum to model templates. The galaxy models used are based on the observed composite $z = 3$ Lyman break galaxy spectrum of Shapley et al. (2003). Two galaxy models are used: one with a strong $\text{Ly}\alpha$ emission line and one with only $\text{Ly}\alpha$ absorption. The fitting routine allows a combination of these models to represent a range in $\text{Ly}\alpha$ strength. IGM absorption is accounted for using the model of Songaila (2004). The galaxy spectrum is multiplied by a power-law to account for the variation in observed UV continuum slope of galaxies. There are a total of four free parameters: normalization, redshift, power-law slope and $\text{Ly}\alpha$ flux. The $\text{Ly}\alpha$ flux was fixed at zero for those galaxies without obvious $\text{Ly}\alpha$ emission in their 2D spectra to avoid over-fitting of noise peaks with the $\text{Ly}\alpha$ line.

Best-fit galaxy models are determined by fitting the models to the observed spectra. The uncertainty on each spectral pixel due to the sky noise is determined from the variance of blank sky pixels in each of the masks. The best fit is determined by the lowest value of the reduced χ^2 . The spectra, along with best fit galaxy models, are shown in Figure 3. The observed spectra, models and sky noise spectrum have been smoothed by 20 pixels (27 Å) for display purposes. Those sources with measurable $\text{Ly}\alpha$

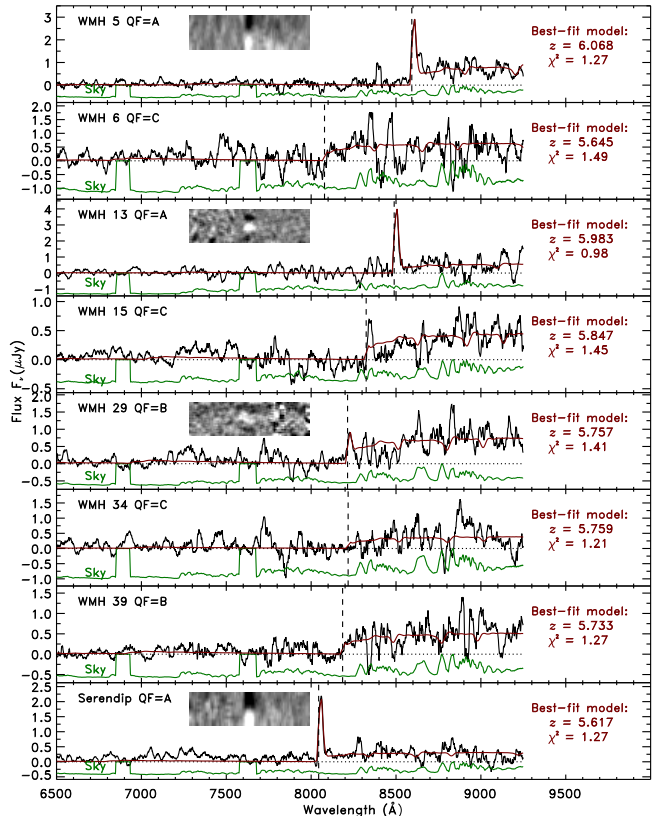


Figure 3. Optical spectra of $z \approx 6$ Lyman break candidates (black) with the best fitting galaxy models (red). The best-fit redshifts and reduced χ^2 are quoted. All spectra are smoothed by 20 pixels (27 Å). Note that template fitting was performed on the unsmoothed spectra. The noise (dominated by the sky) is plotted in green and offset from zero. The noise is not to scale, but included to show when observed spectral features may be due to noise. The dashed lines mark the wavelengths of the $\text{Ly}\alpha$ transition for the best-fit redshifts. For the four LBGs with $\text{Ly}\alpha$ emission the inset panel shows a 220 Å long portion of the 2D spectrum centred on the $\text{Ly}\alpha$ emission. Due to nod-and-shuffle observing mode, these spectra show positive and negative versions offset vertically. WMH 5 and Serendip were observed in multi-slit mode so there is one positive (white) below one negative (black). WMH 13 and WMH 29 were observed in long-slit mode so there is one positive (white) with two negative (black) above and below.

emission have an inset panel in Figure 3 with a 220 Å long segment of the 2D spectrum centred on the $\text{Ly}\alpha$ emission.

3.3. Results of spectroscopy

Each target has a redshift *Quality Flag* in Table 2 which gives a measure of the confidence of the redshift determined. The categories follow those in Vanzella et al. (2009) where ‘A’ means unambiguous, ‘B’ is likely and ‘C’ is uncertain. Strong $\text{Ly}\alpha$ emission was only found in two of the $z \approx 6$ galaxies, WMH 5 and WMH 13. These are assigned QF=A. In addition, weak, but still significant, $\text{Ly}\alpha$ was observed in WMH 29 which is assigned QF=B. Note that this $\text{Ly}\alpha$ line at $z = 5.757$ is in a region of very low sky noise. It is doubtful that such a line would have been significantly detected at slightly higher redshift. Due to the weakness of this line it cannot be determined if it is asymmetric and therefore definitely $\text{Ly}\alpha$. If it is instead [O II] at $z = 1.20$ then the 4000 Å break would be expected at 8790 Å, whereas the continuum break is observed to be at < 8500 Å. The apparent

emission line at 8400 \AA in WMH 15 in Figure 3 is found to be due to sky lines upon examination of the full resolution spectrum.

One of the serendipitous mask-filling galaxies with photometric redshift $z > 3.5$ was also found to have strong Ly α at $z = 5.618$, just below the redshift range of our sample. It is labeled ‘‘Serendip’’ and is the last object in Table 2 and Figure 3. It has QF=A and is located at 02:26:37.02 –04:55:20.4. This galaxy has $i' - z' = 1.1$, well below our selection criterion of $i' - z' = 2.0$. The reason for this much lower color is that the strong Ly α line is still within the i' filter at this redshift. When an emission line of this strength shifts from the i' band to the z' band (at $z \approx 5.8$) it increases the $i' - z'$ color by 0.5.

All four of the galaxies with Ly α emission show significant spectral breaks across the Ly α line. All four have best fit galaxy spectra at redshifts equal to their Ly α redshifts. This is not too surprising for those three with strong Ly α lines, because inability to fit the line would increase the χ^2 . However it is encouraging for WMH 29, which has only weak Ly α , where the continuum break contributes most of the weight in the fit. For the four galaxies without Ly α emission, we depend upon continuum breaks to constrain the redshift. WMH 39 also shows a break at $z = 5.73$ and is assigned QF=‘B’ based on this break. WMH 15 shows a likely continuum break between $z = 5.85$ and $z = 5.95$, however this break is not so clear as that in WMH 39 leaving the redshift uncertain and hence QF=‘C’.

The other two galaxies, WMH 6 and WMH 34, show continuum flux in the z' band and regions with no flux at shorter wavelength, but the exact break redshifts are not well-constrained, so are assigned QF=‘C’. These two spectra have the highest noise (along with WMH 13 which has the strongest Ly α line) which likely accounts for the lack of a clear redshift solution. The best fit redshift of $z = 5.645$ for WMH 6 is quite unlikely given its color of $i' - z' = 2.1$ (see Section 6.1). We note that in any color-selected sample there is a possibility for rare interlopers with unusual colors (e.g. Capak et al. 2011; Hayes et al. 2012) to masquerade as high-redshift galaxies. However, based on the evidence we have and the stringent color cuts, we expect there to be very few of these in our sample. Only WMH 13 out of the seven color-selected spectroscopic targets has a Ly α line with rest-frame equivalent width $> 25 \text{ \AA}$ giving a fraction of 14%. This is comparable to the fraction of $20 \pm 8\%$ for luminous $z \sim 6$ LBGs found by Stark et al. (2011) and lower than the $54 \pm 21\%$ observed by Curtis-Lake et al. (2012).

Table 2 includes the absolute magnitudes, M_{1350} of the galaxies. These were calculated from the z' band magnitudes after taking account of the observed Ly α emission line contributions. At these redshifts, the z' band contains flux at or very close to rest-frame 1350 \AA and hence the main uncertainty on the absolute magnitudes comes not from k -corrections, but the z' band photometry and is $\approx 10\%$. With absolute magnitudes ranging from -21.67 to -22.65 , the spectroscopic targets are some of the most luminous LBGs known at $z \sim 6$. For comparison, the break in the $z \approx 6$ luminosity function is at $M_{1350} = -20.2$ (Bouwens et al. 2007). WMH 5 has $M_{1350} = -22.65$, which is even more luminous than the

lowest known luminosity $z \approx 6$ quasar, CFHQS J0216-0455 ($M_{1450} = -22.21$, Willott et al. 2009). WMH 5 is only 2.1 arcsec from the center of a galaxy in Figure 1. This is an inclined disk galaxy with a photometric redshift of $z = 1.01$, rest-frame B -band absolute magnitude of $M_B = -21.5$ and disk half-light radius 4 kpc. Using the results of studies of the Tully-Fisher and similar relations for $z = 1$ disk galaxies (Dutton et al. 2011; Miller et al. 2011), we find the circular velocity for this galaxy should be $\approx 160 \text{ km s}^{-1}$. Modeling the gravitational potential as an isothermal sphere, the gravitational lensing magnification of WMH 5 due to this galaxy is a factor of 1.27. Hence the intrinsic absolute magnitude of WMH 5 is still extremely luminous with $M_{1350} \approx -22.4$.

4. GALAXY SIZES

An important cosmological observation is that galaxies are smaller at higher redshifts than similar galaxies at lower redshift (Ferguson et al. 2004; Bouwens et al. 2004). This is expected due to the evolution in the virial radii of dark matter halos, but the exact nature of the evolution also depends upon details of gas accretion, retention and star formation efficiency. The faint $z \sim 6$ galaxies discovered in GOODS and HUDF typically have half-light radii of ≈ 0.1 arcsec (equivalent to 0.6 kpc; Bouwens et al. 2006) and are therefore not expected to be resolved in typical seeing-limited, ground-based observations. Table 1 showed that the measured z' band FWHM of many CFHTLS $z \approx 6$ LBGs are larger than the seeing of ≈ 0.7 arcsec of the images.

Four (WMH 14, WMH 15, WMH 16 and WMH 29) of the 40 LBGs (including two with spectroscopy) are located within the CANDELS survey and therefore have high-resolution *Hubble Space Telescope* ACS and WFC3 imaging available (Grogin et al. 2011; Koekemoer et al. 2011). We have retrieved these data in order to get a more detailed view of the galaxy morphologies for this small sub-sample. The WFC3 F125W and F160W images are shown in Figure 4. We have used GALFIT (Peng et al. 2010) to fit galaxy models to the main galaxy component in each filter independently. The best fit single model galaxy and the residuals after subtraction are also plotted in Figure 4. Similar models and residuals are found for both filters in all cases, providing a high degree of confidence in the model galaxy fits. Inspection of the F814W images showed that the residuals have similarly red F814W-F125W colors as the main galaxies, indicating the residuals are at $z \approx 6$ and not at lower redshift.

For WMH 14 the residual emission is compact and coincident with the main galaxy. For the other three galaxies, the residual emission is more extended and clumpy, extending at least an arcsec (equivalent to 6 kpc) from the main galaxy centroid. This is suggestive of galaxy mergers and interactions being common in the most luminous galaxies at this epoch. The model galaxies have a wide range of half-light radii from only 0.3 and 0.5 kpc for WMH 14 and WMH 29, respectively, to 1.0 and 1.5 kpc for WMH 15 and WMH 16, respectively.

Six of the 15 galaxies in D2 are well-detected in the ACS F814W observations of the COSMOS field. They are all spatially resolved and half of them show multiple components. The F814W filter extends further redward than the CFHT i' filter, so such detections in F814W are consistent with the $z \approx 6$ LBG classification. The

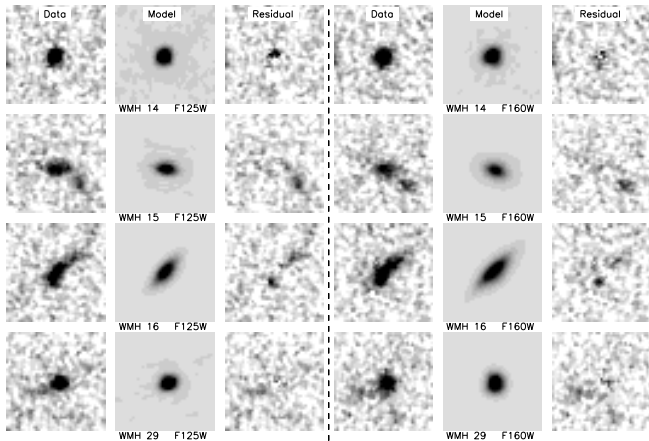


Figure 4. WFC3 F125W (left) and F160W (right) imaging of the four LBGs in the CANDELS survey. For each observation there are three panels shown from left to right: (i) the data; (ii) the GALFIT best fit single galaxy model; (iii) the residuals after subtraction of the smooth galaxy profile. All images are 2.4 arcsec across, corresponding to a linear physical size of 14 kpc. The images of WMH 29 are oriented at an angle of 50° counter-clockwise to the standard north-up, east-left orientation of the other three galaxies. For all galaxies, there are significant residuals with similar structure in the two filters. In the case of the lower three galaxies these residuals reveal multiple components interacting with the main galaxies.

frequent occurrence of multiple components in both the WFC3 and ACS data indicate that about half of the LBG sample have signs of interactions/mergers.

The only size data available for the full sample are the measured FWHM in the z' band. Figure 5 plots FWHM against magnitude for the 40 LBGs and 27 brown dwarfs. The brown dwarfs are included as a comparison sample, because they are expected to be almost all unresolved. Although many brown dwarfs exist in binary systems (Burgasser et al. 2007) only a small fraction would have the relevant component separations to appear as a single, resolved source in these images. The spread in observed FWHM for dwarfs is due to three factors: the small difference in quality between the four Deep fields, the variation in stellar FWHM from the field centers to the edges and photometric noise. The photometric noise is evident by the increased spread in FWHM for dwarfs at fainter magnitudes. It is for this reason that we use the dwarfs as the unresolved comparison sample to compare to the LBGs rather than stars at brighter magnitudes.

Figure 5 also shows the 25%, 50% and 75% centiles of the measured FWHM distribution as a function of magnitude for simulated point sources inserted into the data (see Section 6.1). The observed distribution for the dwarfs agrees well with the simulation. Note that the three dwarfs with measured FWHM > 1 arcsec all have FWHM ≈ 0.6 in J band imaging with higher S/N than z' band for these red sources, confirming photometric noise as the reason for a small fraction of large FWHM values. It is found that 3 out of 20 (15%) dwarfs with magnitudes in the range of LBGs are observed to have FWHM > 1 arcsec and lie beyond the 75% simulated centile due to noise. In contrast, we find that 26 out of the 40 LBGs (63%) have FWHM > 1 arcsec and that the same percentage lie beyond the 75% centile. Assuming that 15% of these LBGs are outliers due to noise, then there remain $\approx 50\%$ which are truly resolved in our ground-based imaging.

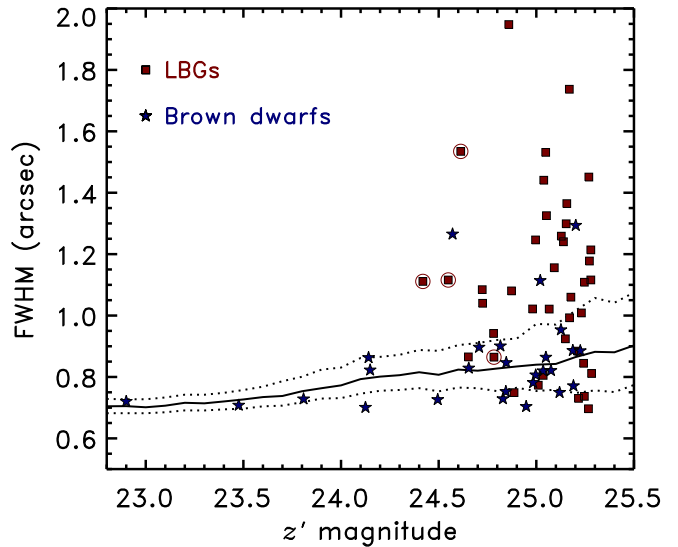


Figure 5. Observed size of the selected Lyman break galaxies (red squares) and brown dwarfs (blue stars). It is evident that the Lyman break galaxies tend to have larger sizes than the unresolved brown dwarfs. The solid line shows the median measured FWHM for artificial point sources added to the images in our completeness simulations (see Section 6.1). The typical measured FWHM of point sources increases at faint magnitudes due to noise. The 25% and 75% quartiles are shown with dotted lines. The distribution of brown dwarfs is consistent with these lines, whereas about 50% of the LBGs are truly spatially resolved. The spectroscopically confirmed LBGs (QF='A' or 'B'; Section 3) are enclosed by a larger circle. Three of these four are spatially resolved.

Given the uncertainty in the broadening of the FWHM values by seeing and noise, it is not possible to reliably deconvolve each value to determine the intrinsic size distribution of our LBG sample. However, a typical intrinsic half-light radius of 2 kpc (0.35 arcsec) is required to observe a galaxy with FWHM 1.1 arcsec (median for our LBG sample) when the FWHM of a point source would be 0.85 arcsec (50% centile for the simulated point sources with magnitude $z' = 25.0$). This contrasts with the typical half-light radius of 1 kpc for $z = 26$ galaxies in GOODS (Bouwens et al. 2006). The high-resolution WFC3 imaging of four LBGs showed that one is compact, one has a compact core with low surface brightness extended emission and two have relatively large half-light radii plus extended emission. This suggests that both large galaxy sizes and multiple emission components are common in our sample of the most luminous LBGs. Our finding is consistent with an extension to the brightest galaxies of the strong correlation between UV luminosity and linear size at $z = 6$ presented by Dow-Hygelund et al. (2007).

5. STACKED GALAXY PROPERTIES

In order to check that the typical LBG properties match those of high-redshift galaxies and to get an idea of the typical galaxy spectral shape, we have stacked the photometric data at the positions of the $z \approx 6$ galaxies. After registering the images, the median flux of each pixel was determined since it provides the most robust estimator that is least affected by outliers (White et al. 2007). Because the near-IR data from VISTA has an extra filter (Y) and is deeper than WIRDS, we just use the 23 galaxies in D1 and D2 with VISTA data.

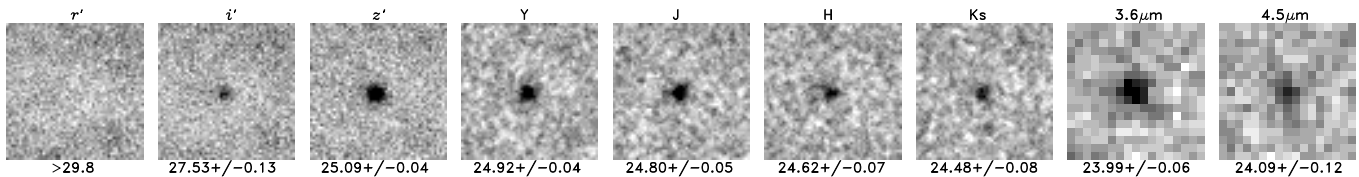


Figure 6. Median stacked images in the $r'i'z'YJHKs$ and IRAC $3.6\mu\text{m}$ and $4.5\mu\text{m}$ filters at the positions of the LBGs used to construct the stacks. There are 23 galaxies in the optical (CFHTLS) and $YJHK$ (VIDEO and UltraVISTA) stacks and 15 in the IRAC bands (S-COSMOS). Each image covers $10'' \times 10''$. The images are oriented with north up and east to the left. Negative holes in the central five arcsec of the images (particularly apparent in r' and i') are due to incompleteness of our LBG sample due to foreground contamination.

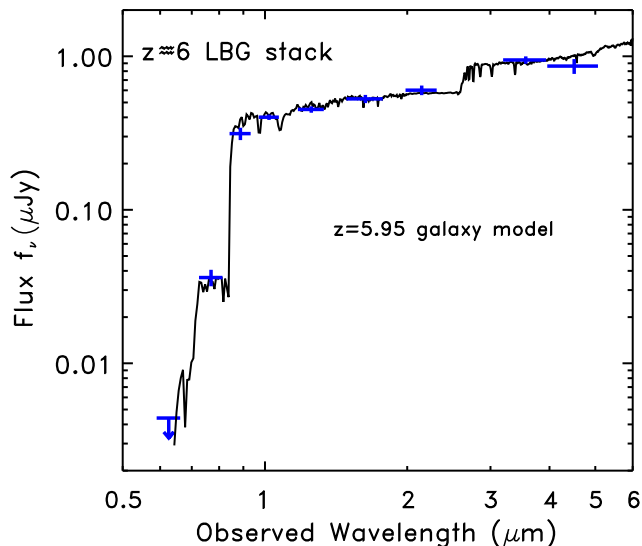


Figure 7. Photometry from the stacked images (blue points with error bars) plotted with stellar evolution synthesis model (black line). The z' band flux has been reduced by a factor of 1.1 to account for the typical $\text{Ly}\alpha$ emission, which is not included in the models. The galaxy model has constant star formation rate, solar metallicity and a Chabrier IMF. The best-fit parameters are redshift $z = 5.95$, stellar mass $= 1.1 \times 10^{10} M_{\odot}$, age $= 1.3 \times 10^8$ yr, star formation rate $= 110 M_{\odot}\text{yr}^{-1}$ and reddening $A_V = 0.75$. See text for further details.

We have checked that the stacked optical and near-IR magnitudes for D3 and D4 are consistent. Deep *Spitzer Space Telescope* IRAC data is available for the 15 galaxies in D2 from the S-COSMOS survey (Sanders et al. 2007). We include these data because these wavelengths are important for constraining the stellar mass and age, but the reader should remember that the IRAC points only correspond to a subset of the objects used for the $r'i'z'YJHKs$ stacks.

The resulting median stacked images are shown in Figure 6. There are significant detections at all filters except for r' band. Photometry of the ground-based data was performed to obtain 3 arcsec aperture magnitudes or limits. These are equivalent to total magnitudes, within the uncertainties. These 3 arcsec apertures are larger than the 2 arcsec used previously in this paper for individual object magnitudes (many of which had low S/N necessitating small apertures) and provide a better match to the IRAC apertures. For the IRAC data which has a broader PSF, 3.8 arcsec apertures were used and a PSF correction to total magnitudes applied. Smoothing of the images showed that for all the optical filters, there is a negative “hole” in the background covering the central five arcsec-

onds. This is most apparent for r' and i' in Figure 6. This is showing us that our $z = 6$ galaxy sample is incomplete. The CFHTLS Deep r' and i' band data is so deep that it is close to the confusion limit and we are missing $z = 6$ galaxies that have foreground galaxies contaminating the photometry aperture in r' and i' . Another consequence of this is that we are unlikely to have strongly gravitational lensed galaxies in our sample due to the lensing galaxy contaminating the source galaxy aperture. Photometric measurements were performed carefully to ensure that the appropriate background level was set. The measured magnitudes of the stacks are given below the images in Figure 6. The 2σ limit on the r' band magnitude (determined from the noise in the background pixels because this region has lower variance than the rest of the field which was populated by galaxies in the input images) gives $r' > 29.8$. This is almost 5 magnitudes fainter than the z' band magnitude and provides compelling evidence that these galaxies are truly at $z \approx 6$ rather than lower redshift galaxies or dwarf stars. The stack colors of $i' - z' = 2.44 \pm 0.14$ and $z' - J = 0.29 \pm 0.06$ are plotted in Figure 2 and are entirely consistent with a typical $z = 5.9$ galaxy.

Figure 7 plots the stack fluxes as a function of wavelength. The z' flux has been reduced by a factor of 1.1 to account for the typical $\text{Ly}\alpha$ emission line contribution. It is apparent that the $YJHKs$ fluxes are described by a power-law with index (defined as $f_{\lambda} \propto \lambda^{\beta}$) redder than $\beta = -2$ (which would be flat on this plot which uses f_{ν}). A power-law fit to the $YJHKs$ fluxes gives $\beta = -1.44 \pm 0.10$, where the 1σ uncertainty comes from 1000 bootstrap resample trials. To ensure that this result is not an artifact of the stacking method, we have also fitted the $YJHKs$ fluxes of the 23 LBGs individually. Excluding two extreme outliers which have poor fits, it is found that the mean $\beta = -1.38$ and the median $\beta = -1.02$. The standard error on the mean is ± 0.20 .

The value of β found is significantly redder than the typical values previously observed for the most luminous $z \approx 6$ LBGs in deep *Hubble Space Telescope* surveys of $\beta = -1.78 \pm 0.11$ (Bouwens et al. 2012), $\beta = -2.10 \pm 0.16$ (Dunlop et al. 2012), $\beta = -2.04 \pm 0.17$ (Wilkins et al. 2011) and $\beta = -2.05 \pm 0.11$ (Finkelstein et al. 2012). Finkelstein et al. showed that although at $z \approx 6$ there is only a weak correlation between β and UV luminosity, there is a stronger correlation between β and stellar mass. Whilst this is not surprising, because in a UV flux-limited sample, a redder galaxy model will require a higher stellar mass, the typical value of β for their most massive bin (10^9 to $10^{10} M_{\odot}$) is -1.78 and the typical stellar mass of our sample is $10^{10} M_{\odot}$ (see below). The simplest explanation for dust in luminous galaxies comes from combining the metallicity–dust, mass–metallicity and mass–

luminosity correlations. Therefore our typical $\beta = -1.4$ for $z \approx 6$ luminous LBGs is not at odds with the work of Finkelstein et al. Our findings suggest that a substantial number of these galaxies have significant dust reddening.

Galaxy models were fitted to the stacked photometry using the photometric redshift method of McLure et al. (2011). The fitted models used Bruzual & Charlot (2003) stellar populations with the Chabrier IMF and the Calzetti et al. (2000) dust attenuation law. Various star formation histories were fitted, but none were preferred at a high significance. Therefore we quote the constant star formation rate results, since these most-luminous LBGs are unlikely to be observed in a state of rapidly declining or increasing star formation rate. Figure 7 shows the best-fit model and its parameters. The best fit redshift was found to be $z = 5.95$ with a 2σ range of $5.87 < z < 5.97$. The best-fit metallicity is solar. The best-fit stellar mass, M_* , is $1.1 \times 10^{10} M_\odot$ with a 2σ range of $4 \times 10^9 < M_* < 1.9 \times 10^{10} M_\odot$. The age and star formation rate are obviously degenerate with the star formation history and dust reddening, so no strong constraints could be placed on those parameters. As was found in the analysis of β , the UV spectral slope is fairly red and this requires significant dust reddening. The best fit has dust extinction of $A_V = 0.75$ and the 2σ range is $0.48 < A_V < 1.48$.

6. GALAXY LUMINOSITY FUNCTION

6.1. Completeness

There are a number of factors that affect the completeness of the sample, or equivalently, the effective volume of the survey. Firstly, the sample does not contain every object brighter than a certain z' magnitude limit due to incompleteness in the source detection algorithm close to the limit. In addition, blending with brighter objects becomes an issue in ground-based data at these faint magnitudes. As was shown in the stacks of Section 5, there is evidence for incompleteness of the sample due to foreground contamination at i' band which prevents some true high-redshift galaxies from having $i' - z' > 2$ in their aperture magnitudes.

In order to determine the effective sky area surveyed, we have carried out an analysis of insertion and recovery of simulated sources into the data. As found in Section 4, about 50% of the $z = 6$ LBGs are spatially resolved, whereas 50% are consistent with point sources. The simulated sources have a similar distribution of observed FWHM to the LBGs. The selection criteria for recovery are identical to those of the automated candidate selection. In addition, we check whether there is a contaminating object at i' band which would cause the observed $i' - z'$ color to fall below the threshold. Figure 8 shows the effective sky area surveyed in all four Deep fields as a function of the input magnitude of the artificial galaxies. The dashed line shows the effective area if one does not consider the foreground contamination of the $i' - z'$ color. The effective area declines slowly from $z' = 23$ to $z' = 24.8$ and then falls more rapidly to $z' = 25.5$. Note that the effective area is still considerable for input magnitudes $25.3 < z' < 25.5$, so some galaxies fainter than the nominal magnitude limit will be in the sample due to photometric scatter.

The next factors to consider for completeness are the

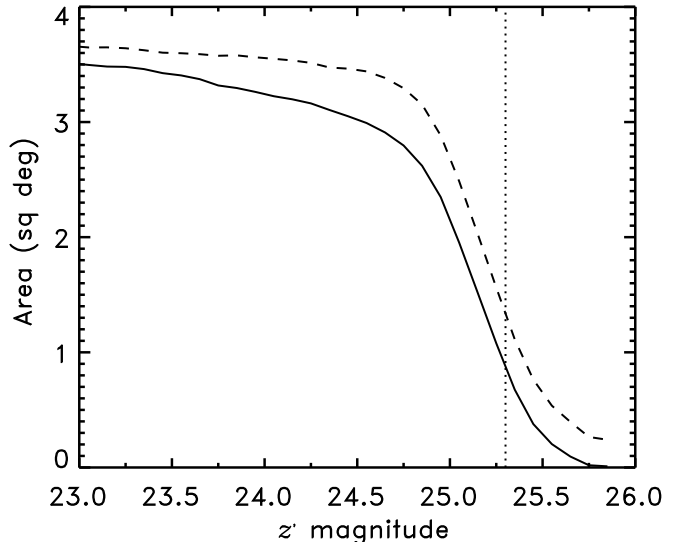


Figure 8. Effective survey area of the LBG sample as a function of magnitude (solid line). Note that these magnitudes are the true magnitudes of the simulated galaxies before photometric noise is added, so some galaxies fainter than the magnitude limit ($z' = 25.3$; dotted line) are included in the sample. The dashed line shows what the effective area would be without incompleteness due to foreground contamination of the i' band magnitude and hence color.

effects of the $i' - z' > 2$ color criterion and the conversion from z' magnitude to absolute magnitude. These are assessed by considering the range of properties expected for high-redshift galaxies, including Ly α emission line strength, UV continuum spectral slope and IGM absorption of the UV continuum. As in Section 3 we use the $z = 3$ LBG composite of Shapley et al. (2003) as the basis for the galaxy template. Absorption shortward of Ly α due to foreground neutral hydrogen is modeled as in Willott et al. (2010) using the mean and scatter derived by Songaila (2004).

A range of UV spectral slopes is implemented, as required by observations. At $z \approx 6$ and high luminosity the reported typical value in the literature is $\beta = -2$ (Bouwens et al. 2012; Finkelstein et al. 2012). Our stacking and individual LBG fitting results showed that for even more luminous $z \approx 6$ LBGs, the typical $\beta = -1.4$. Combining our results with other work, we assume a typical value for the population of $\beta = -1.8$ and a Gaussian distribution with 1σ scatter of 0.5. We have checked and using a mean of $\beta = -1.5$ or $\beta = -2$ makes no difference to our results.

Several spectroscopic studies have investigated the distribution of Ly α equivalent widths at high redshifts. We combine the works of Stark et al. (2011), Curtis-Lake et al. (2012) and our own work in Section 3 to derive a Ly α rest-frame equivalent width probability distribution for luminous $z \approx 6$ LBGs of $P(W_{\text{Ly}\alpha}) \propto \exp(-W_{\text{Ly}\alpha}/25)$. This is similar to the exponential parameterization of Dijkstra & Wyithe (2012), also based on the data of Stark et al.

A sample of 500 simulated galaxies were generated with properties randomly drawn from these distributions and their $i'z'J$ colors and absolute magnitudes, M_{1350} , determined if located at all redshifts between $z = 5.5$ and

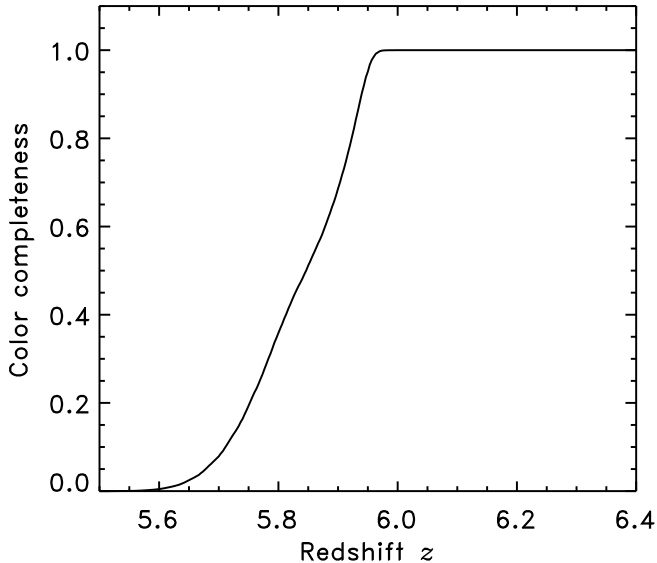


Figure 9. Completeness due to the color criterion of $i' - z' > 2$ as a function of redshift. This curve was determined for a population of galaxies with Ly α equivalent width, UV continuum slope, IGM absorption and photometric errors as described in the text. Because all objects with $i' - z' > 2$ have been identified as either galaxies or brown dwarfs there is no high redshift cutoff in completeness corresponding to high $z' - J$ colors.

$z = 6.7$. Photometric scatter in the colors is also included. The median $i' - z'$ and $z' - J$ color as a function of redshift is plotted in Figure 2. This curve runs very close to the stacked values of $i' - z'$ and $z' - J$, suggesting the models are indeed a good representation of the data. At redshifts $5.6 \leq z \leq 6$, some fraction of galaxies are too blue in $i' - z'$ to be included in the sample. In particular, we find that galaxies with strong Ly α lines at $z < 5.9$ are much less likely to be included in our sample than those with weak Ly α lines. This could be the reason why we find a relatively low Ly α fraction for the galaxies with best-fit redshifts $z \approx 5.8$ (c.f. Curtis-Lake et al. 2011). At $z > 5.9$, where this bias does not exist, the fraction with strong Ly α in our sample is quite high (two out of three). Figure 9 shows the completeness as a function of redshift due to the color selection criterion.

6.2. Magnitude distributions

Before using these data to derive the $z = 6$ galaxy luminosity function, we consider simply the observed z' band magnitude distributions of the galaxies and brown dwarfs. Figure 10 shows these two distributions. The dwarf magnitudes extend to $z' = 22.8$ and have a fairly flat distribution with a peak at $z \approx 25.0$. This flat distribution is a consequence of galactic structure and the survey completeness as a function of magnitude. At magnitude $z' = 25$, mid-L and mid-T dwarfs are 500 and 200 pc away, respectively. The CFHTLS fields are at high galactic latitude and hence the space density of brown dwarfs declines beyond the disk. The galaxy distribution is quite different and much steeper. There are no galaxies brighter than $z' = 24.4$ and almost 70% of the galaxies lie in the small magnitude range of $25 < z' < 25.3$. The steepness of this distribution, despite the declining survey completeness at faint magnitudes, is due to the very steep bright end of the galaxy luminosity function.

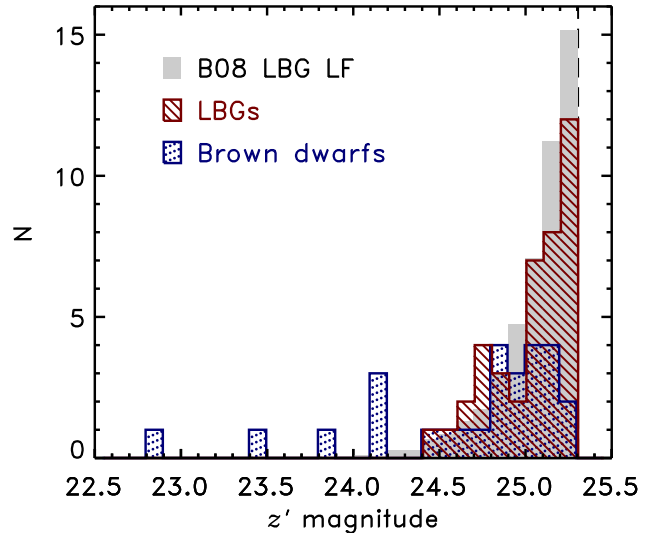


Figure 10. Magnitude histograms for Lyman break galaxy candidates and brown dwarfs selected by colors $i' - z' > 2$ and $z' \leq 25.3$. The brown dwarf magnitude distribution (blue, dotted) has a fairly shallow slope due to the fact that the distance to L dwarfs is well beyond the disk scale length. The galaxy magnitude distribution (red, diagonal line) has a very steep slope. The gray shaded histogram shows the expected LBG counts for our survey based on the known luminosity function which is well-constrained at fainter magnitudes (Bouwens et al. 2008). The dashed black line shows the magnitude limit of our samples.

The gray histogram in Figure 10 shows the expected magnitude distribution for $z = 6$ LBGs in our survey based on the evolving luminosity function in Section 5.3 of Bouwens et al. (2008). At $3.5 < z < 6.5$ this luminosity function is constrained by the LBG luminosity functions determined in Bouwens et al (2007) based on ACS observations in the GOODS, HUDF and HUDF-Parallel fields. The expected counts take into account the selection criteria, completeness and photometric uncertainty of our sample. It is clear from Figure 10 that both the shape and overall normalization of the expected counts are close to those observed in our sample. This is remarkable given that our survey volume is 40 times greater than that used by Bouwens et al. (2007) and hence their data contained very few sources as bright as ours. The expected magnitude distribution predicts 46 LBGs in our sample, compared with 40 observed. The number expected at $z' < 25$ is 13, identical to that observed.

6.3. Luminosity function derivation

Because our LBG sample covers only a limited range of apparent and absolute magnitudes, we cannot use it to determine the full galaxy luminosity function at $z = 6$. The luminosity function at the break and at fainter magnitudes has already been well-studied from deep *Hubble Space Telescope* surveys over small sky areas (Bouwens et al. 2007). The main contribution of our study is to determine the space density of very rare, highly luminous LBGs.

Due to the fact that most CFHTLS LBGs have unknown redshifts (within the Lyman break redshift selection range) and unknown k -corrections due to Ly α emission line contribution and spectral slope, we can-

Table 3
Luminosity function of $z \approx 6$ LBGs from CFHTLS

| M_{1350} | Φ ($\text{Mpc}^{-3} \text{mag}^{-1}$) | Φ_{low} ($\text{Mpc}^{-3} \text{mag}^{-1}$) | Φ_{high} ($\text{Mpc}^{-3} \text{mag}^{-1}$) |
|------------|-------------------------------------------------|--------------------------------------------------------------|---------------------------------------------------------------|
| -22.5 | 2.66×10^{-8} | 9.08×10^{-9} | 7.78×10^{-8} |
| -22.0 | 2.18×10^{-6} | 8.70×10^{-7} | 9.70×10^{-6} |
| -21.5 | 1.45×10^{-5} | 2.88×10^{-6} | 2.92×10^{-5} |
| -21.0 | 1.29×10^{-4} | 7.06×10^{-5} | 2.19×10^{-4} |
| -20.5 | 2.30×10^{-4} | 9.34×10^{-5} | 5.77×10^{-4} |

^a Φ_{low} and Φ_{high} are the lower and upper bounds for each absolute magnitude node containing 68% of the bootstrap results.

not map a particular apparent magnitude onto an absolute magnitude and redshift. Therefore we cannot carry out standard luminosity function derivation methods where each observed source corresponds to a point on the redshift, luminosity plane or by counting the number of galaxies in luminosity bins. Instead we use the stepwise maximum-likelihood method of Efsthathiou et al. (1988) where the luminosity function is characterized by values in a number of absolute magnitude bins. We choose to use 5 regularly spaced nodes at $M_{1350} = [-22.5, -22, -21.5, -21, -20.5]$ since this covers the full extent of the absolute magnitude range of our detected LBGs and ensures that extrapolation of the luminosity function beyond this range will not bias our results.

The comparison of the model with the data is performed in observed magnitude space because this is the only way of accounting for the selection effects and completeness discussed in Section 6.1 and the non-unique mapping of apparent to absolute magnitude. For a model luminosity function (defined as power-laws connecting and extending beyond the five nodes), the completeness information and photometric noise are used to generate a model observed z' magnitude distribution, using the same method as in Section 6.2. These model magnitudes are binned in $\delta z' = 0.1$ magnitude bins, n_{mod} , and compared to the observed z' magnitude histogram, n_{obs} , (Figure 10). The data are Poissonian and the likelihood, \mathcal{L} , of observing the data given the model over all N magnitude bins is given by

$$\mathcal{L} = \prod_{i=1}^N \frac{e^{-n_{\text{mod},i}} n_{\text{mod},i}^{n_{\text{obs},i}}}{n_{\text{obs},i}!}. \quad (1)$$

The galaxy space densities at the five nodes are the five free parameters which are adjusted using an amoeba algorithm (Press et al. 1992) to determine the maximum likelihood. The 68% range on the best fit values are determined via bootstrapping by 400 trials of Poisson perturbation of the $n_{\text{obs},i}$ values.

The results are given in Table 3. Figure 11 plots the data and compares with previous results from the literature. Our best-fit values match well the Schechter parameterizations of Bouwens et al. (2007, 2008) and McLure et al. (2009) and agree with previous binned values determined by Bouwens et al. (2007) and McLure et al. (2009). Our two most luminous data points show the step decline in space density towards high luminosity required by our data. The 68% uncertainties on our data points are fairly large due to the small sample size and

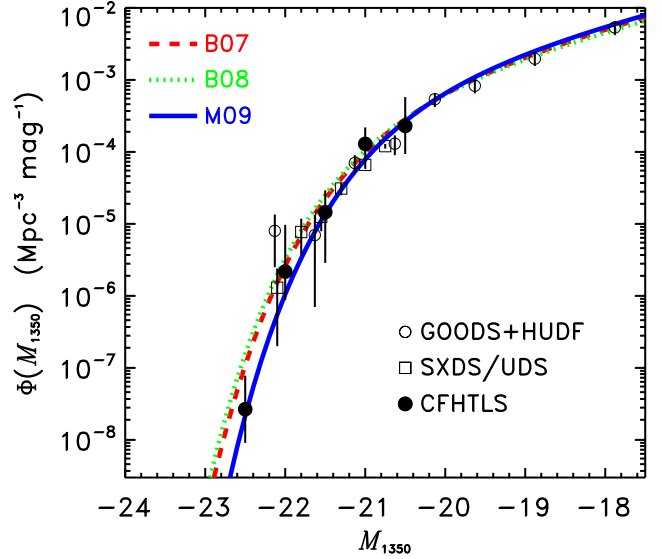


Figure 11. Galaxy luminosity function at $z \approx 6$. The maximum likelihood node points determined in this paper from CFHTLS are shown by filled black circles, whilst binned points from the literature are shown with open black symbols (GOODS+HUDF from Bouwens et al. 2007 and SXDS/UDS from McLure et al. 2009). Schechter function curves are plotted from the works of Bouwens et al. (2007) (red), Bouwens et al. (2008) (green) and McLure et al. (2009) (blue). The CFHTLS data at the bright end most closely match the McLure et al. derivation.

the fact that sources can be redistributed to neighboring nodes in different trials. The total volume of our survey is $\approx 10^7$ Mpc. Therefore we are not truly measuring a space density of $< 10^{-7} \text{Mpc}^{-1}$ at $M_{1350} = -22.5$. The low value of this node is showing that there must be a sharp decline brighter than $M_{1350} = -22$ or else we would observe more bright LBGs. One of our spectroscopically confirmed galaxies, WMH 5, has $M_{1350} = -22.65$, but most of the rest have absolute magnitudes close to $M_{1350} = -22$, in agreement with this sharp decline in number density.

6.4. Field-to-field variance

Part of the robustness of our results comes from the fact the CFHTLS Deep is spread over four separate 1 square degree fields. We now consider the variance in $z \approx 6$ LBG counts across the four fields. We identified 8, 15, 8 and 9 LBGs in D1, D2, D3 and D4, respectively. The two fields with the least certain identifications due to shallower J -band (D3 and D4) do not have an unusual number of counts, providing confidence in the LBG classification in these fields. The field with the largest deviation is D2 (COSMOS) which, with 15 LBGs, is 1.6σ beyond the mean, assuming Poisson variance only. Another source of variance is the large-scale distribution of matter, so called cosmic variance. This could be important if the most luminous LBGs are hosted by rare, massive dark matter halos. We use the cosmic variance calculator of Trenti & Stiavelli (2008) assuming a duty cycle of 0.5 for the halos. For this space density and duty cycle the minimum dark matter halo mass hosting a galaxy is $2 \times 10^{12} M_{\odot}$. The variance calculation shows that the cosmic variance contribution to the total variance in each field is expected to be only half the Poisson

variance contribution. Hence including cosmic variance the D2 field is 1.4σ beyond the mean and not unexpectedly overdense.

As well as chance, another factor that could be contributing to the higher counts in D2 is that the CFHTLS data is a little shallower in that field. With shallower data, there are three possible effects that alter the expected number of candidates found: (i) the larger magnitude uncertainties cause more objects to scatter in from faintward of the $z' = 25.3$ magnitude limit; (ii) the larger magnitude uncertainties cause more objects to scatter in from blueward of the $i' - z' = 2$ color limit; (iii) the detection completeness will be lower at the faint end. All of these effects are included for the sample as a whole in Section 6.1, but we do not analyze them on a field-by-field basis. Certainly, effect (i) is not significant because comparison of the CFHTLS z' and Subaru z' magnitudes in D2 shows that only two of the 15 have Subaru $z' > 25.3$. A similar fraction is found for D1 using VIDEO Z magnitudes and is expected based on Figure 8. We do not have similar comparison data to determine the likely strength of effects (ii) and (iii) (which affect the number of candidates in opposite directions). Therefore we ascribe the higher number of LBGs in D2 being mostly due to chance and the total of 40 in the sample is unbiased and fully accounted for by our selection function.

6.5. Discussion

Our results show that there is a sharp decline in the $z \approx 6$ galaxy space density for galaxies brighter than $M_{1350} = -22$, consistent with the exponential function of Bouwens et al. (2007; 2008). The steepness of this function is much steeper than that of the dark matter halo mass function for the expected host halo masses, M_H , of these luminous LBGs ($10^{12} < M_H < 10^{13} M_\odot$; Lee et al. 2009; Trenti et al. 2010). This implies suppression of star formation in the most massive halos at high redshift. The galaxy luminosity and dark matter halo mass functions can be related using the conditional luminosity function (CLF) method (Yang et al. 2003). At low redshifts, the bright end of the galaxy luminosity function is consistent with the relationship $L \sim M_H^{0.28}$ (Vale & Ostriker 2006). The physical explanation for this is likely feedback from an AGN and/or inefficient gas cooling in high mass halos (Benson et al. 2003).

Because our best-fit luminosity function is so similar to that of Bouwens et al. (2007), we can adopt the $z = 6$ CLF derivation of Trenti et al. (2010) which was fit to this function. Trenti et al. (2010) showed that by requiring only recently formed (200 Myr) halos to host LBGs, the duty cycle for high mass halos must be almost unity, unlike the values of $\approx 20\%$ previously estimated for typical LBGs at this epoch (Stark et al. 2007; Lee et al. 2009). Under this assumption that the duty cycle does not vary much over the luminosity range of interest, Trenti et al. (2010) showed that the high luminosity end of the CLF follows a relationship of $L \sim M_H^{0.5}$. This is somewhat steeper than is found at low redshift, but still indicates that luminosity is a slowly varying function of halo mass.

Models with star formation efficiency and duty cycle (or star formation timescale) which are independent of halo mass do not predict such a steep decline in the luminosity function at the brightest magnitudes (Stark et

al. 2007; Muñoz & Loeb 2011). These works were able to fit the $z = 6$ luminosity function of Bouwens et al. (2007) because those data did not provide evidence of the sharp exponential decline. Our results show that the same process that limits star formation in high mass halos at low redshift is also acting at a time just one billion years after the Big Bang.

7. CONCLUSIONS

We have performed the largest area survey for luminous LBGs at $z \approx 6$. These galaxies have been used to study their physical sizes and spectral energy distributions. The large sky area has enabled the most robust results on the space density decline at the bright end of the luminosity function. Below we list the specific conclusions drawn from this work.

- Spectroscopy of seven galaxies revealed redshifts for four of them. Three of these have Ly α emission lines, one of which is extremely weak with $W_{Ly\alpha} = 4\text{\AA}$. All four galaxies show continuum redward of Ly α which enables redshift determination from the break location.
- About half of the LBGs are resolved in the ground-based CFHT imaging observations. This is consistent with a typical intrinsic half-light radius for luminous $z \approx 6$ galaxies of 2 kpc, higher than the typical 1 kpc in GOODS. High resolution imaging of a subsample shows that some galaxies have a dominant component with large half-light radii and some have multiple components. A larger sample with high resolution imaging is necessary to determine if there is a relationship between interaction frequency and star-formation rate.
- The properties of the stacked photometry have been investigated. These data show a flux decrement in the observed-frame optical of nearly 100 due to the Lyman break. The $YJHK$ photometry are fit by a power-law of slope $\beta = -1.44 \pm 0.10$, much redder than for less luminous galaxies at this epoch. The stacked SED is well fit by a $z = 5.95$ constant star formation model with mass $\approx 10^{10} M_\odot$. Significant dust reddening is required ($A_V = 0.75$) showing that dust is more prevalent in the most massive systems, again possibly due to these being merger-induced starbursts.
- The magnitude distributions of our LBG sample and a $i' - z'$ color-matched sample of L/T dwarfs are considered. Whilst the dwarfs have a fairly flat distribution with a peak at $z' \approx 25$, the LBGs have a distribution that rises sharply with magnitude. Our $z \approx 6$ luminosity function derivation provides clear evidence for a sharp decline in space density brighter than $M = -22$.
- The decline in space density at high luminosity is consistent with a relationship between galaxy luminosity and dark matter halo mass of $L \sim M_H^{0.5}$. This shows that the processes limiting star formation in high mass halos at low redshift are also operating effectively at a time just 1 billion years after the Big Bang.

This paper is dedicated to the memory of Steve Rawlings, who taught CJW to look for the signal in the noise. Thanks to Genevieve Soucail for providing reduced near-IR data for some of our targets. Thanks to the anonymous referee for suggestions that considerably improved the paper. Based on observations obtained with MegaPrime/MegaCam, a joint project of CFHT and CEA/DAPNIA, at the Canada-France-Hawaii Telescope (CFHT) which is operated by the National Research Council (NRC) of Canada, the Institut National des Sciences de l'Univers of the Centre National de la Recherche Scientifique (CNRS) of France, and the University of Hawaii. This work is based in part on data products produced at TERAPIX and the Canadian Astronomy Data Centre as part of the Canada-France-Hawaii Telescope Legacy Survey, a collaborative project of NRC and CNRS. We gratefully acknowledge use of data from the ESO Public Survey programs 179.A-2005 and 179.A-2006 with the VISTA telescope. This work uses observations taken by the CANDELS Multi-Cycle Treasury Program with the NASA/ESA HST, which is operated by the Association of Universities for Research in Astronomy, Inc., under NASA contract NAS5-26555. Based on observations obtained at the Gemini Observatory, which is operated by the Association of Universities for Research in Astronomy, Inc., under a cooperative agreement with the NSF on behalf of the Gemini partnership: the National Science Foundation (United States), the Particle Physics and Astronomy Research Council (United Kingdom), the National Research Council (Canada), CONICYT (Chile), the Australian Research Council (Australia), CNPq (Brazil) and CONICET (Argentina). This paper uses data from Gemini programs GN-2009A-Q-2, GS-2009A-Q-3, GN-2010B-C-9 and GN-2011A-C-1.

REFERENCES

- Allard, F., & Freytag, B. 2010, *Highlights of Astronomy*, 15, 756
 Barkana, R. & Loeb, A. 2001, *Phys. Rep.* 349, 125
 Barmby, P., Huang, J.-S., Ashby, M. L. N., et al. 2008, *ApJS*, 177, 431
 Benson, A., Bower, R. G., Frenk, C. S., Lacey, C. G., Baugh, C. M., & Cole, S. 2003, *ApJ*, 599, 38
 Bertin, E., & Arnouts, S. 1996, *A&AS*, 117, 393
 Bielby, R., Hudelot, P., McCracken, H. J., et al. 2012, *A&A*, 545A, 23
 Bouwens, R. J., Illingworth, G. D., Blakeslee, J. P., Broadhurst, T. J., & Franx, M. 2004, *ApJ*, 611, L1
 Bouwens, R. J., Illingworth, G. D., Blakeslee, J. P., & Franx, M. 2006, *ApJ*, 653, 53
 Bouwens, R. J., Illingworth, G. D., Franx, M., & Ford, H. 2007, *ApJ*, 670, 928
 Bouwens, R. J., Illingworth, G. D., Franx, M., & Ford, H. 2008, *ApJ*, 686, 230
 Bouwens, R. J., Illingworth, G. D., Oesch, P. A., et al. 2012, *ApJ*, 754, 83
 Bruzual, G., & Charlot, S. 2003, *MNRAS*, 344, 1000
 Bunker, A. J., Stanway, E. R., Ellis, R. S., & McMahon, R. G. 2004, *MNRAS*, 355, 374
 Burgasser, A. J., Reid, I. N., Siegler, N., et al. 2007, in *Protostars and Planets V*, ed. B. Reipurth, D. Jewitt, & K. Keil (Tucson, AZ: Univ. Arizona Press), 427
 Calzetti D., Armus L., Bohlin R., Kinney A., Koornneef J., & Storchi-Bergmann T. 2000, *ApJ*, 533, 682
 Capak, P., Mobasher, B., Scoville, N. Z., et al. 2011, *ApJ*, 730, 68
 Cole, S. 1991, *ApJ*, 367, 45
 Curtis-Lake, E., McLure R. J., Pearce, H., et al. 2012, *MNRAS*, 422, 1425
 Delorme, P., Willott, C. J., Forveille, T., et al. 2008, *A&A*, 484, 469
 Dickinson, M., Stern, D., Giavalisco, M., et al. 2004, *ApJ*, 600, L99
 Dijkstra, M., & Wyithe, J. S. B. 2012, *MNRAS*, 419, 3181
 Dow-Hygelund, C. C., Holden, B. P., Bouwens, R. J., et al. 2007, *ApJ*, 660, 47
 Dunlop, J. S., McLure, R. J., Robertson, B. E., et al. 2012, *MNRAS*, 420, 901
 Dutton, A. A., van den Bosch, F. C., Faber, S. M., et al. 2011, *MNRAS*, 410, 1660
 Efstathiou, G., Ellis, R. S., & Peterson, B. A. 1988, *MNRAS*, 232, 431
 Ferguson, H. C., Dickinson, M., Giavalisco, M., et al. 2004, *ApJ*, 600, L107
 Finkelstein, S. L., Papovich, C., Salmon, B., et al. 2012, *ApJ*, 756, 164
 Finlator, K., Oppenheimer, B. D., & Davé, R. 2011, *MNRAS*, 410, 1703
 Grogan, N. A., Kocevski, D. D., Faber, S. M., et al. 2011, *ApJS*, 197, 35
 Hayes, M., Laporte, N., Pelló, R., Schaerer, D., & Le Borgne, J.-F. 2012, *MNRAS*, 425, L19
 Jarosik, N., Bennett, C. L., Dunkley, J., et al. 2011, *ApJS*, 192, 14
 Jarvis, M. J., Bonfield, D. G., Bruce, V. A., et al. 2012, *MNRAS*, submitted, arXiv:1206.4263
 Jiang, L., Egami, E., Kashikawa, N., et al. 2011, *ApJ*, 743, 65
 Kennicutt, R. C. 1998, *ARA&A*, 36, 189
 Koekemoer, A. M., Faber, S. M., Ferguson, H. C., et al. 2011, *ApJS*, 197, 36
 Lee, K.-S., Giavalisco, M., Conroy, C., Wechsler, R. H., Ferguson, H. C., Somerville, R. S., Dickinson, M. E., & Urry, C. M. 2009, *ApJ*, 695, 368
 Lonsdale, C. J., Smith, H. E., Rowan-Robinson, M., et al. 2003, *PASP*, 115, 897
 McCracken, H. J., Milvang-Jensen, B., Dunlop, J. S., et al. 2012, *A&A*, 544A, 156
 McLure R. J., Jarvis M. J., Targett T. A., Dunlop J. S., & Best P. N., 2006, *MNRAS*, 368, 1395
 McLure R. J., Cirasuolo M., Dunlop J. S., Foucaud S., & Almaini O., 2009, *MNRAS*, 395, 2196
 Miller, S. H., Bundy, K., Sullivan, M., Ellis, R. S., & Treu, T. 2011, *ApJ*, 741, 115
 Muñoz, J. A., & Loeb, A. 2011, *ApJ*, 729, 99
 Nagao, T., Murayama, T., Maiolino, R., et al. 2007, *A&A*, 468, 877
 Peng, C. Y., Ho, L. C., Impey, C. D., & Rix, H.-W. et al. 2010, *AJ*, 139, 2097
 Press, W. H., Teukolsky, S. A., Vetterling, W. T., & Flannery, B. P. 1992, *Numerical Recipes in C: The Art of Scientific Computing* (Cambridge: Cambridge Univ. Press)
 Reylé C., Delorme, P., Willott, C. J., et al. 2010, *A&A*, 522, A112
 Sanders, D. B., Salvato, M., Aussel, H., et al. 2007, *ApJS*, 172, 86
 Scoville, N., Abraham, R. G., Aussel, H., et al. 2007, *ApJS*, 172, 38
 Shapley, A. E., Steidel, C. C., Pettini, M., & Adelberger, K. L. 2003, *ApJ*, 588, 65
 Shimasaku, K., Ouchi, M., Furusawa, H., et al. 2005, *PASJ*, 57, 447
 Songaila, A. 2004, *AJ*, 127, 2598
 Spinrad, H., Stern, D., Bunker, A., Dey, A., Lanzetta, K., Yahil, A., Pascarelle, S., & Fernández-Soto, A. 1998, *AJ*, 116, 2617
 Stark, D. P., Loeb, A., & Ellis, R. S., & Ouchi, M. 2007, *ApJ*, 668, 627
 Stark, D. P., Ellis, R. S., & Ouchi, M. 2011, *ApJ*, 728, L2
 Su, J., Stiavelli, M., Oesch, P., et al. 2011, *ApJ*, 738, 123
 Taniguchi, Y., Scoville, N., Murayama, T., et al. 2007, *ApJS*, 172, 9
 Trenti, M., & Stiavelli, M. 2008, *ApJ*, 676, 767
 Trenti, M., Stiavelli, M., Bouwens, R. J., Oesch, P., Shull, J. M., Illingworth, G. D., Bradley, L. D., & Carollo C. M. 2010, *ApJ*, 714, L202
 Vale, A., & Ostriker, J. P. 2006, *MNRAS*, 371, 1173
 Vanzella, E., Giavalisco, M., Dickinson, M., et al. 2009, *ApJ*, 695, 1163
 White, R. L., Helfand, D. J., Becker, R. H., Glikman, E., & de Vries, W. 2007, *ApJ*, 654, 99
 Wilkins, S. M., Bunker, A. J., Stanway, E., Lorenzoni, S., & Caruana, J. 2011, *MNRAS*, 417, 717
 Willott, C. J., Delorme, P., Reylé, C., et al. 2009, *AJ*, 137, 3541
 Willott, C. J., Delorme, P., Reylé, C., et al. 2010, *AJ*, 139, 906
 Yan, H., & Windhorst, R. A. 2004, *ApJ*, 612, L93
 Yang, X., Mo, H. J., & van den Bosch, F. C. 2003, *MNRAS*, 339, 1057